Direct ink writing of highly bioactive glasses

Amy Nommeots-Nomm[1,2], Peter D. Lee[2], Julian R. Jones[1*]

[1] Department of Materials, Prince Consort Road, Imperial College London, London, SW7 2BP, UK

[2] School of Materials, University of Manchester, Manchester, M13 9PL, UK

Graphical Abstract

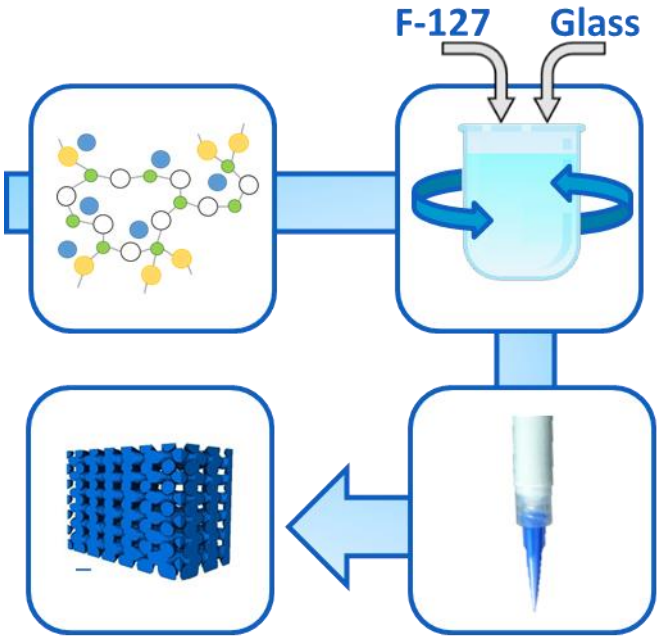

Key words

Robocasting, direct ink writing, scaffold, Bioglass, amorphous, bone repair

Abstract

Direct ink writing (DIW) or Robocasting, is an additive manufacturing technique that offers the opportunity to create patient specific bioactive glass scaffolds and high strength scaffolds for bone repair. The original 45S5 Bioglass® composition crystallises during sintering and until now, robocast glass scaffolds contained at least 51.9 mol% SiO_2 or B_2O_3 to maintain their amorphous structure. Here, ICIE16 and PSrBG compositions, containing < 50 mol% SiO_2, giving silicate network connectivity close to that of 45S5, were robocast and compared to 13-93 composition. Results showed Pluronic F-127 can be used as a universal binder regardless of glass reactivity and that particle size distribution affected the ink "printability". Scaffolds with interconnects of 150 µm (41-43% porosity) had compressive strengths of 32-48 MPa, depending on the glass composition. Robocast scaffolds from these highly reactive bioactive glasses promise greatly improved bone regeneration rates compared with existing bioactive glass scaffolds.

Introduction

Larry Hench's original Bioglass® 45S5 composition [1] was the first material to elicit a chemical bond with bone via its dissolution in body fluid. For regeneration of large bone defects, 3D scaffolds are needed that can guide cell growth and act as a temporary template before biodegrading as the bone repairs [2]. The original Bioglass composition, 45S5 (46.1 mol% SiO_2, 24.4 mol% Na_2O, 26.9 mol% CaO and 2.6 mol% P_2O_5), cannot be made into 3D constructs, while maintaining its amorphous structure, due to its limited thermal processing window between its glass transition and crystallisation temperature. Sintering the 45S5 Bioglass composition produces a glass-ceramic [3] [4]. Filho *et al.* [5] showed that once crystallised, the time taken for the formation of hydroxyapatite (HA) upon the surface of the glass in simulated body fluid (SBF), a marker of bioactivity, increased from 8 h (45S5 in glass form) to more than 24 h (45S5 as a glass ceramic) and resulted in heterogeneous dissolution. Laser spinning maintained the amorphous structure of 45S5 glass, but did not provide structural strength [6]. Consequently, melt-derived glass compositions have been developed that avoid crystallisation during sintering, enabling bioactive glasses to be made into porous constructs, while maintaining their bioactive nature [7-9]. Various processing methods have been developed, such as gel-casting [10] and the foam replica method [11], which create amorphous scaffolds with the morphology of cancellous bone. The scaffolds produced had high porosities ~80%, and suitable interconnects between 100-150 µm but had limited mechanical strengths up to 10 MPa [10, 12].

The development of the 3D printing technique known as robocasting or direct-write assembly (DIW) has enabled the production of bioactive glass scaffolds with strengths within the range of cortical

bone [13-15], summarised in Table 1. This processing method enables the formation of scaffolds with grid-like structures of straight channels, creating open porosities in x, y, and z. The robocasting process relies on dispersing glass powder into a suitable binder, to formulate an ink. The ink chemistry, glass particle size, distribution and packing affect the quality of the green body and consequent mechanical properties of the final scaffold. The ink must meet a variety of criteria to be suitable for robocasting: it must exhibit shear thinning rheology to flow easily through a fine diameter nozzle under force then be self-supporting once extruded and it must allow drying without cracking of the filaments. The ink should also be able to accommodate high particle loading and the binder must burn out below the glass transition temperature of the glass composition used [16-18].

To date, three polymeric binders have been used to robocast bioactive glasses; Pluronic F-127, ethyl cellulose/ polyethylene glycol, and carboxymethyl cellulose (Table 1) [3, 13, 14, 19, 20]. The first robocasting paper published for bone applications was by Franco *et al.* [21] using calcium phosphate with Pluronic F-127 surfactant as a carrier ink, which was since used with bioactive glasses of 13-93 (54.6 mol% SiO_2, 22.4 mol% CaO, 6 mol% Na_2O, 1.7 mol% P_2O_5, 7.9 mol% K_2O, 7.7. mol% MgO) and 13-93B (54.6 mol% B_2O_3, 22.4 mol% CaO, 6 mol% Na_2O, 1.7 mol% P_2O_5, 7.9 mol% K_2O, 7.7. mol% MgO) compositions [14]. Pluronic F-127 is a water soluble block co-polymer surfactant with thermally reversing rheological behaviour, consisting of poly(ethylene oxide)-poly(propylene oxide)-poly(ethylene oxide) tri-blocks (PEO-PPO-PEO) ($HO(C_2H_4O)_a(C_3H_6O)_b(C_2H_4O)OH$). Ethyl cellulose/ polyethylene glycol, and carboxymethyl cellulose are two alternative binders which rely on processing in ethanol instead of water reducing premature ionic released during processing.

Another key factor in the robocasting process is related to the size of the particulate and its distribution. To robocast bioactive glasses, the mean particle size used in literature previously has been between 1-5 µm, enabling extrusion through nozzles as fine as 30 µm [21]. Glass particle sizes in this range are usually achieved by attrition milling in a solvent, commonly ethanol, as bioactive glasses begin to dissolve on contact with water [3, 14, 15]. A wide particle distribution allows the formulation of higher particle loaded inks, by allowing rearrangement and slippage of particles during printing [21, 22]. Wide distributions also allow for better, more intimate packing of the particles within the scaffold struts, resulting in denser filaments post sintering. While smaller particles sinter more rapidly, due to their higher specific surface area, crystallisation is surface nucleating and therefore the higher surface area also promotes lower onset of crystallisation temperatures.

The glasses which have been robocast to date, (with the exception of 45S5) all had above 50 mol % network formers within their compositions pushing their modified network connectivity (NC') values

above 2.31. The network connectivity of a glass is the mean number of bridging oxygen bonds (-Si-O-Si-) per silicon atom, and its value is suggested to be a measure or predictor of the bioactivity of the composition [23]. The maximum network connectivity is 4 (fused silica) and as network connectivity decreases, dissolution rate and bioactivity increase. The hypothesis is that the network connectivity of 45S5 Bioglass, 2.11, is most suitable for rapid bone regeneration. Previous work on gel-cast foamed scaffolds using these glass compositions showed that ICIE16 with the closest network connectivity to 45S5 precipitates HCA within 48 h, with 13-93 precipitate by 1 week. PSrBG showed to precipitate a strontium substituted layer by 2 weeks [24].

The aim of this work was to investigate if two low silica (< 50 mol %) content bioactive glasses PSrBG (44.50 SiO_2, 4.0 Na_2O, 4.0 K_2O, 7.5 MgO, 17.80 CaO, 17.80 SrO, 4.5 P_2O_5 in mol%) and ICIE16 (49.46 SiO_2, 36.27 CaO, 6.6 Na_2O, 1.07 P_2O_5 and 6.6 K_2O, in mol%), which were designed to have NC' values closer to that of 45S5 Bioglass (Table 2), could be robocast into 3D porous scaffolds and maintain their amorphous glass structure. 13-93 was also printed as a bench mark to compare with current literature. A second aim was to determine whether Pluronic F-127 can be used as a universal binder for bioactive glasses independent of their reactivity and composition.

*Table 1: Summary of published robocasting glass and ink combinations, 6P53B (51.9 SiO_2, 19 CaO, 9.8 Na_2O, 2.5 P_2O_5, 1.8 K_2O , 15 MgO, in mol%), 13-93 (54.6 SiO_2, 22.4 CaO, 6 Na_2O, 1.7 P_2O_5, 7.9 K_2O , 7.7 MgO in mol%), 13-93B3 (54.6 B_2O3, 22.4 CaO, 6 Na_2O, 1.7 P_2O_5, 7.9 K_2O , 7.7 MgO in mol%). *Calculated assuming magnesium is a network modifier, not a former, due to its compositional dependency **crystalline post sintering ***values not reported and therefore, measured using ImageJ from the published SEM images available.*

Glass used		6P53B [20]	13-93B3	13-93 [14]	13-93 [13]	45S5 [3, 19]**
Network Connectivity*		2.53	2.58		2.58	2.11
Particle Size D_{50}	/µm	1.2	2.1	2.2	≈ 1	Range 1-10 (D_{50} not stated)
Glass loading	/Vol %	30	45		40	45
Ink chemistry *Dispersant*		F-127 *water*	Ethyl cellulose/ polyethylene glycol *ethanol*		F-127 *water*	Carboxymethyl cellulose *ethanol*
Strut Size	/µm	100	300 ± 20		330	250- 300***
Pore Size	/µm	500	420 ± 30		300	Not available
Porosity	/%	60	48 ± 3		47	63 ± 3

Compressive strength /MPa	136 ± 22	65 ± 11	142 ± 20	87± 9	13 ± 1

Methodology

Table 2: Compositional summary of the glasses used and their relative network connectivity

Oxide: /mol%	SiO_2	CaO	Na_2O	P_2O_5	K_2O	MgO	SrO	Density /gcm^{-3}	Modified Network Connectivity
ICIE16	49.46	36.6	6.6	1.07	6.6			2.74	2.13
13-93	54.6	22.4	6	1.7	7.9	7.7		2.50	2.58
PSrBG	44.5	17.8	4	4.5	4	7.5	17.8	3.07	2.31

The three glass compositions (Table 2) were produced via melt quenching using high purity silica (SiO_2) (High Purity, Prince Minerals, Stoke-on-Trent), phosphorus pentoxide (P_2O_5) and the carbonate equivalent of the modifying oxides required, all reagents were purchased from Sigma Aldrich UK. Precursors were mixed for 8 h using a mini roller (Wheaton UK), then melted at 1400 °C for 2 h, in a 95% platinum 5% gold crucible. The melt was then quenched into deionized water. The frit was then collected, and dried at 100°C. Once dried it was then milled using two different processing techniques:

Ball Mill: The frit was separated into 25 g batches, ground for 6 minutes at 500 rpm using Fritsch Premium Line 7 ball mill, using 80 ml grinding bowls with nine 15 mm tempered steel balls. Glass powders were then sieved to < 32 µm using a Russell Finex compact sieve shaker with ultrasonic deblinder.

Jet mill: Glass frit was pre-ground for 1 minute at 500 rpm using a Fritsch Premium Line 7 ball mill. Frit was then jet milled in 50 g batches using a Picojet 40AFG Hosokawa Alpine jet mill with a gas pressure of 5 PSI, a classifier speed was between 5000- 8000 depending upon the glass processed. All internal parts were ceramic lined to limit contamination and abrasion during use.

Particle Size measurements: Particle size was measured using a Malvern Mastersizer 2000 (Malvern Instruments Ltd. UK). To form stable suspensions suitable for measurement, glass powders were dispersed in water using a sonicator, and ethylene glycol was added to aid dispersion. Refractive index values used were glass: 1.54, water: 1.33, ethylene glycol: 1.44.

Ink preparation: 20, 25 and 30 wt% Pluronic F-127 solutions were prepared prior to use and kept in a fridge at 5 °C. Small batches were mixed in individual pots, using a planetary centrifugal mixer

(Thinky mixer ARE-250 USA) to reduce mixing time and prevent overheating. Glass additions were made step wise in vol%, using values of 20, 30, 40 and 50 vol% glass loading, calculated using the relative glass densities. Inks were mixed on the 'mixing' setting for 4 minutes at 2000 rpm, then 'degassed' for 2 minutes at 1800 rpm. Once mixed, inks were cooled, in a 5°C fridge for 15 minutes, before more glass was added and remixed. This was repeated until all glass was incorporated. Prior to the final mix, 1 wt% of octanol-1 was added; inks were the cooled and transferred to printing syringes, which were sealed and run on a 2 minute 'degass' prior to use.

Robocasting: Printing was completed using a robocaster system (3dInks, USA) onto acetate sheets. Conical nozzles of various internal diameters of 250, 410 and 580 µm were used to print all parts in this work. Scaffolds were designed using the built in RoboCAD 3.0 (3DInks, USA) software. A nozzle dependent length of ink (known as the 'lead-in') was extruded prior to scaffold printing to ensure flow was homogenous within the printed part. During printing the humidity was controlled at 60-80% and temperature held at 23 °C.

Rheological studies were completed using a TA Instruments Discovery HR-1 rheometer fitted with a 40 mm parallel plate geometry, a solvent trap to prevent drying and a Peltier plate for temperature control. Solutions were prepared and pipetted between the two plates, the geometry was then closed to a 1 mm gap and the excess material extruded was removed. Flow tests were conducted at 25 °C, 30 second pre-test temperature soak, at strain rates between 0.02-200 s^{-1}, dynamic mechanical analysis was carried out at a frequency of 1 Hz with stresses between 0.1- 3000 Pa. The phase lag, δ, between peak applied shear stress and peak shear strain was determined automatically by the equipment's software over 10 oscillations.

Extrusion was simulated by extruding syringes of ink fitted into a custom frame, using a Zwick/Roell z2.5 mechanical testing machine. A constant displacement was applied to the plunger within the syringe to simulate set printing speeds determined by the extrusion ratio.

Compression testing: 10 scaffolds 6 x 6 x 6 mm with parallel faces were tested under compression using a Zwick/Roell z2.5 machine fitted with a load cell of 10 kN and strain rate of 1 mm min^{-1}.

X-ray diffraction (XRD): Glasses were ground into a fine powder prior to analysis. Patterns were collected using a Bruker D2 PHASER desktop X-ray diffractometer with a step size of 0.0345°, 10 s per step, measuring between 5 and 80 degrees 2θ. The radiation source was Ni filtered CuKα.

Scanning Electron Microscopy (SEM): Low magnification images of the scaffold topography were collected using the JEOL JSM 5610 LV with a working distance of 10-12 mm. Samples were mounted onto conductive stubs using carbon tape sputter coated in gold using an Emitech K550 for two

minutes at 25 mA. Due to the porous nature of the scaffolds one side was painted with silver to increase the conductivity of the samples. Scaffolds were also fractured using compression testing to study internal strut structure and formation. Images were taken using a voltage of 5 kV to reduce charging of the samples.

Micro-CT: Micro-CT was conducted on the i13 beam line at the Diamond Light Source, Didcot, UK. Images were collected using the PCO. Edge 5.5 camera at 10 x magnification, using pink beam radiation with a 5 mm I.D. gap. This gave a field of view 0.83 x 0.70 mm and corresponding pixel size of 0.33 µm. A 2 mm aluminium and 950 µm chromium filter were used. An exposure time of 0.045 s with 4001 projections. The data was processed using Avizo FEI software, a region of interest of 750 x 750 x 750 was selected, a non-local means filter was applied, and the data was thresholded to calculate internal strut porosity volumetrically.

Results and discussion

Particle Size

Previous studies used a particle size for robocasting between 1-5 µm. Glasses of three compositions, ICIE16, PSrBG, and 13-93 were produced via both ball and jet milling. Ball milling relies upon using tempered steel balls which are spun at high speeds within a chamber made of the same material. As the balls collide with the glass frit the particles fracture and their size is reduced. After ball milling, glasses were sieved using a vibrasonic sieve to less than 32 µm. In comparison, jet milling is a one-step grinding and sieving processing method. It uses air pressure to energise particles into colliding against one another and fracture, reducing their size. A classifier then spins at a user selected speed and separates particles depending upon their size; the faster it spins, the smaller the particles that are collected. This process is ideal for producing bioactive glass particles as it can obtain particles of small sizes and narrow distribution in one step, without the need for secondary sieving. It is also advantageous as it is a dry grinding method which avoids the needs for wet processing, commonly used to obtain small particle sizes, which could lead to surface reactions upon the glass altering bioactivity via premature ion release. An example of the particle morphology and distribution created by the two milling methods is summarised in Figure 1, particle size characterisation is summarised in Table 3. The jet mill process formed smaller diameter particles with a narrower distribution; this led to agglomeration of the powders. The particle surfaces appeared to be smoother compared with the ball milled equivalents (Figure 1c). The ball milled glasses had a much broader size distribution, with greater surface topography, but SEM images suggest they have a lower aspect ratio than their jet milled equivalents.

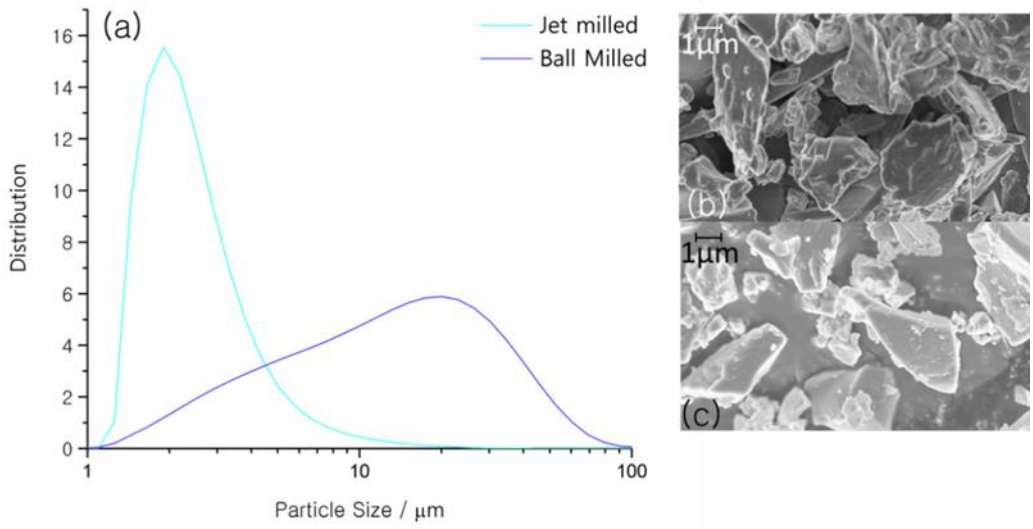

Figure 1: Example of (a) particle size distribution data, and SEM images of ICIE16 glass (b) ball milled, and (c) jet milled.

Table 3: Particle size distributions of each glass composition when processed via jet milling and ball milling, with D_{10}, D_{50} and D_{90} representing the diameter at the 10th, 50th and 90th percentile.

Glass Composition	Ball Milled $D_{10}/D_{50}/D_{90}$ /µm	Jet Milled $D_{10}/D_{50}/D_{90}$ /µm
13-93	3.3/10.8/30.5	1.4/1.9/3.7
ICIE16	3.2/15.8/39.5	1.5/3.6/12.1
PSrBG	3.1/12.5/35.0	2.8/5.1/18.2

Simulating robocasting:

Robocasting can be simulated via compression testing [21]. The relationship between particle size and force needed to extrude was studied using inks made of up ICIE16 glass at various volume fraction ratios. Inks were made with 25 wt% Pluronic F-127 and then with 45 and 50 vol% of ICIE16 ground via jet or ball milling. The results are shown in Figure 2. It is thought that particle loaded inks form a three phase profile within the printing nozzle: an unyielding core which moves at constant velocity, which is surrounded by a yielded shell experiencing laminar flow, with slip happening at the outer layer by the nozzle walls. This behaviour was dependent upon the particle distributions and their ability to slip and rearrange themselves within the nozzle itself during printing. When milling bioactive glasses, via any method, their volume is not spherical therefore their behaviour within the nozzle will not be idealised as described. Due to their variation in aspect ratio they are more likely to arrange in the direction of the loading as shown by robocast filaments [25].

The inks formulated with a glass loading of 45 vol% behaved very differently to inks with 50 vol% glass. At 45 vol%, inks that contained both the jet milled and ball milled glass reached their stabilisation force (the force at which steady state flow is achieved) at similar times, highlighted by the grey dashed lines. Even though they had a smaller particle size, the jet milled inks needed greater forces to be extruded through the equivalent diameter nozzles. This suggests that the distribution of the jet milled glasses was too narrow to allow intimate packing within the nozzle, preventing slipping and rearrangement [14, 26-28]. This hypothesis is supported in Figure 1 and Table , which showed that the particle distribution of the ball milled glasses was much greater than the jet milled sample.

When the glass loading within the inks was increased to 50 vol%, the forces needed to extrude the ink containing jet milled glass was over double that of inks containing 45 vol% of glass. This suggests that the distribution of the particles had a greater effect than the particle size itself on ink formation and printability. The larger particle size and wider distribution created via ball milling produced inks that were easier to print but take longer to reach a stabilised printing force; the opposite was seen with the smaller sized jet milled particles.

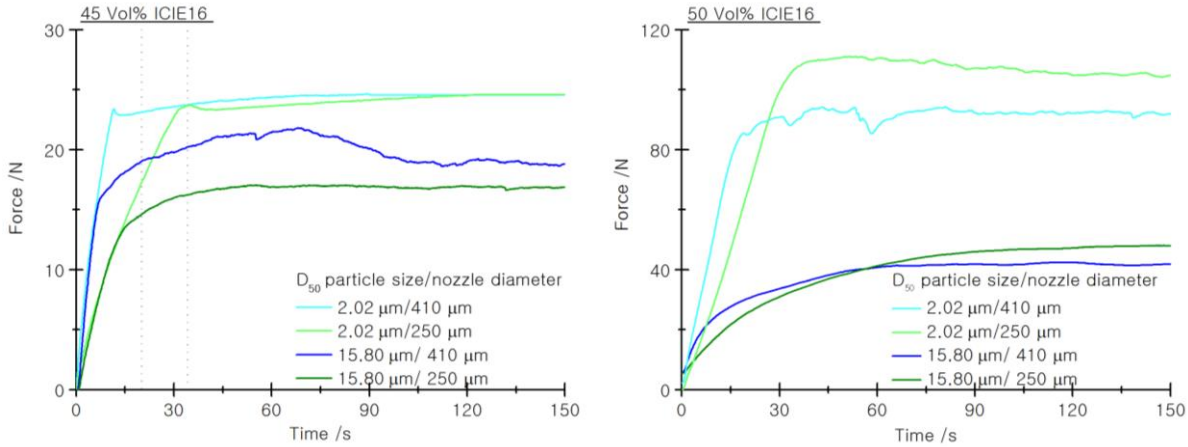

Figure 2: Effect of particle size, and milling method, on the force and time needed to reach stabilisation during simulated robocasting via compression testing of 20 wt % Pluronic F-127 (in water) inks loaded with 45 and 50 vol% of ICIE16 glass particles.

Sintering:

The three glasses were formulated into trial inks with 45 vol% glass in at 25 wt % F-127 solution to investigate the effect of particle size on sinterability. Previous work [29] optimised the sintering profile for these three glass compositions manufactured via ball milling into gel-cast foamed scaffolds. The same sintering protocols were applied to inks containing glasses produced via both jet and ball milling. XRD patterns are shown in Figure 3 with reference to unprocessed glass particles.

226 Thermal processing of 13-93 is well characterised within literature [30]. Fagerland *et al.* reported a
227 thermal processing window, the temperature range between glass transition and crystallisation
228 onset, of 188 °C for particles between 300-500 µm and that crystallisation was surface nucleating.
229 Literature shows that for particle sizes as small at 1- 5 µm the 13-93 composition could be sintered
230 for 1 h at 700 °C without crystallisation occurring, which was also seen here [20].

231 Previous work showed that for ball milled particles, ICIE16 and PSrBG needed to be sintered for 1.5 h
232 at 690 °C, and 5 h at 700 °C respectively to gain adequate viscous flow to produce mechanically
233 strong scaffolds. The reduction in particle size, produced via jet milling, resulted in crystallisation
234 occurring prematurely. Due to the challenges associated with quantifying the amount of crystallinity
235 obtained during sintering and the need for reproducibility, a key aim for this work was to maintain
236 the glasses' amorphous nature. To maximise the compressive strengths of the scaffolds via sintering
237 optimisation, without crystallisation occurring, to maintain the highly bioactive nature of the
238 compositions, it was deemed that the larger particle size range, produced by ball milling, was
239 needed.

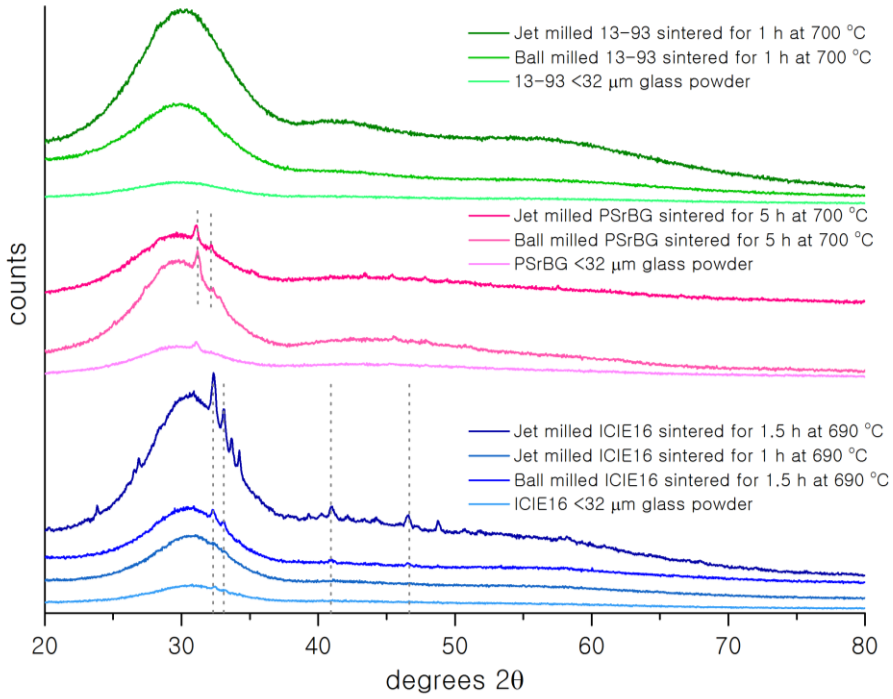

240

241 *Figure 3: Effect of particle size on crystallisation of ICIE16, PSrBG and 13-93 robocast scaffolds studied via XRD, grey dotted*
242 *lines highlight the crystallisation peaks. The crystalline phase present in ICIE16, was found to be* $Na_{4.24}Ca_{3.8}$ *(*Si_6O_{18}*) 01-078-*
243 *1650. Due to their low intensity and limited number, peaks in PSrBG were not identified.*

Ink optimisation

Pluronic F-127 can form stable suspensions with inorganic particles when dissolved in water via steric repulsion by forming Van der Waals and hydrogen bonds with –OH groups on particle surfaces. At low temperatures it forms a low viscosity solution due to the adsorption of water onto the PPO segments of the copolymer, allowing the chains to slide across each other. Above its gelation temperature, the polymer chains rearrange themselves to form micelle aggregates due to the adsorption of water on these segments becoming energetically unfavourable. The release of water molecules and the reduction of hydrogen bonding between the water and the –OH groups of the hydrophobic PPO segments results in the reversible formation of a viscous gel, which is strong enough to keep particles in suspension, and be able to support multiple layers printed upon one another [31].

A particle loaded ink properties can be modelled using the Herschel-Bulkley model equation 1 [32].

$$\tau = \tau y + K\dot{\gamma}^{n} \quad (1)$$

Where K is the viscosity parameter, and n is the flow index. Inks loaded with increasing volume fractions of glass were studied (Figure 4a). For all inks studied $n < 1$ (equation 1), if $n < 1$, an ink is reported to be shear-thinning, with viscosity reducing when the ink is subjected to increasing shear; making it suitable for robocasting [15, 21, 31, 33, 34].

Conrad *et al.* showed that the average shear rate within the nozzle can be approximated to 50 s^{-1} [35]. Consequently, viscosity-shear rate studies were completed and the viscosity at 50 s^{-1} was measured; the results for all three glass compositions are presented in Figure 4b. The viscosity of Pluronic F-127 at 25 wt% without glass addition was 11.81 Pa s. Viscosity increased as the glass loading within the ink increased from 20 to 50 vol %. At maximum loading (50 vol % glass), the viscosity for all three glasses was within 76.3 ± 2.2 Pa s. Regardless of the composition of the glass, the results followed the same trend, suggesting that Pluronic F-127 was a suitable binder, independent of glass composition.

Figure 4c shows the relationship between gelation temperature and volume fraction of glass within the ink. 25 wt % of Pluronic F-127 without glass gelled at 19.8 °C, similar to values reported by Feilden *et al.* [36] . At 20 vol% glass, the gelation temperature was similar to that of pure 25 wt% Pluronic F-127 of 20.6 ± 0.2 °C. As glass addition within the ink increased to 45 vol%, the gelation temperature dropped to 6.40 ± 0.8 °C, perhaps due to the increasing level of disruption created within the network with increasing glass loading. Pluronic F-127 gels due to the release of water molecules from the PPO group within its structure. Premature gelation suggests that the glass

preferentially bonds the water molecules, taking up the water before it is energetically favourable to be released. Consequently, accelerating gelation by allowing the PPO groups to hydrophobically associate at lower temperatures. As glass concentration increased, this process happened more readily. This phenomenon has a consequent effect on the processability of the inks, as gelation occurs more readily at higher glass loading and so it is harder to incorporate all of the glass powder, and to gain a homogenous mix without air bubble entrapment.

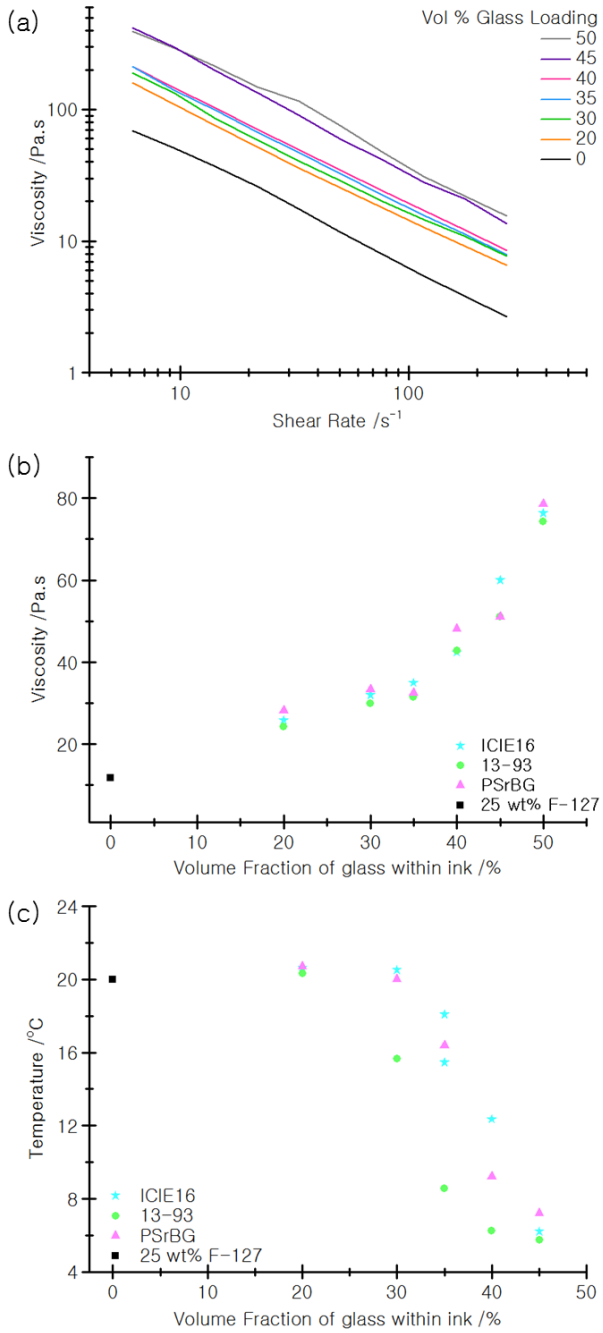

Figure 4: (a) Viscosity of inks as a function of shear rate with inks made with 20-50 vol% of ICIE16; (b) viscosity of 25 wt% Pluronic F-127 based inks as a function of glass loading for inks made with ball milled ICIE16, PSrBG, and 13-93 glass,

measured at 25 °C a shear rate of 50 s^{-1}; (c) gelation temperature 25 wt% Pluronic F-127 based inks as a function of glass loading for inks made with ball milled ICIE16, PSrBG, and 13-93 glass, measured at 25 °C a shear rate of 50 s^{-1}.

Scaffold preparation

Figure 5 shows sintered robocast scaffolds made from ICIE16, PSrBG and 13-93 using 45 vol% of glass with 25 wt% of Pluronic F-127. Figure 5a-c shows the structure of the green bodies of the scaffolds as printed. The green bodies produced were mechanically robust, enabling easy removal from the printing substrate, without the need to print into an oil bath. Figure 5c shows a sectioned surface of a strut from a green body. As highlighted by the image the binder fully coated the glass particles, and porosity can be seen between them. Figure 5d and e show scaffolds as sintered, showing a good degree of sintering was achieved with all three glass compositions, with struts maintaining their as printed geometries with uniform shrinkage in the xy direction.

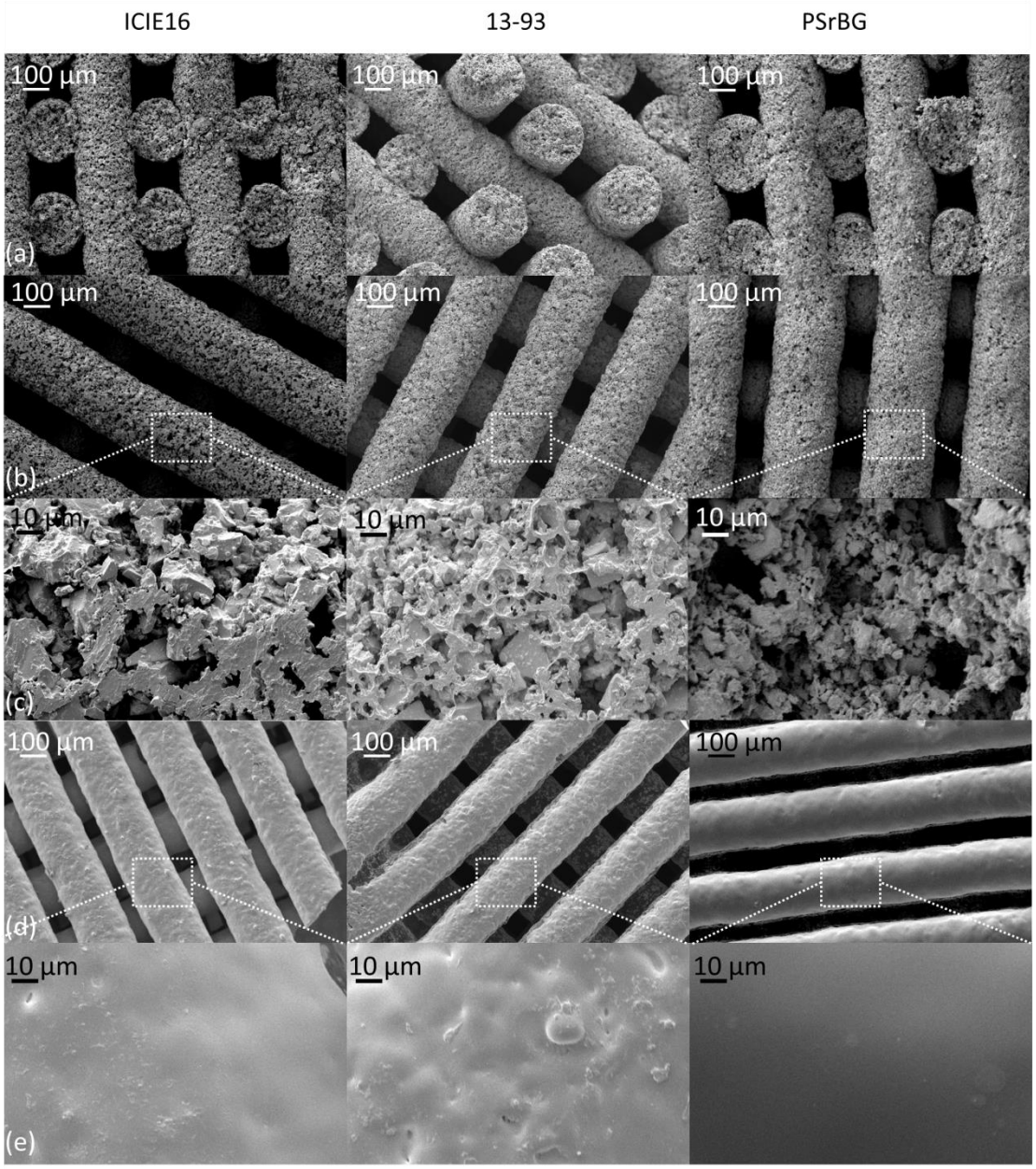

Figure 5: SEM images of ICIE16, 13-93 and PSrBG robocast scaffolds: (a-c) green bodies prior to sintering, (d-e) post sintering. Row (a) images are cross sections of struts in the z direction, row (b) are struts in x-y, row (c) images show examples of the particle packing, row (d) images are scaffolds post sinter, row (e) higher magnification of surface post sinter.

Shrinkage

Scaffolds were printed from all three glasses with the same ratio of glass volume to binder, 25 wt% F-127 and 45 vol% glass. Their shrinkage was then compared, pre and post sintering, when printed through a 410 µm nozzle (Table 4).

Table 4: Shrinkage of printed scaffolds in x, y and z axis, measurements as volume %, 6 scaffolds of each compositions were printed through 3 nozzle diameters (250, 410 and 610 µm).

Direction	13-93	PSrBG	ICIE16
x	26.71 ± 0.05	23.38 ± 0.02	28.54 ± 0.02
y	27.57 ± 0.06	23.76 ± 0.03	26.72 ± 0.03
z	21.31 ± 0.04	18.02 ± 0.06	18.84 ± 0.05

Shrinkage in x and y was homogeneous for all glass compositions, with ICIE16 shrinking the most followed by 13-93 and then PSrBG. All shrinkage in the z direction was less than that of x and y, which is surprising, as during sintering the z direction experiences the load of the scaffold and x and y do not. For PSrBG and ICIE16, shrinkage in the z direction was similar, between 18-19%, which was less than that of 13-93 (21.3%). Li *et al.* [13] and Deliormanli *et al.* [14] both reported shrinkages of 13-93 through a 410 µm nozzle of between 24-26 %, which is within the same range seen in this work.

Compression testing

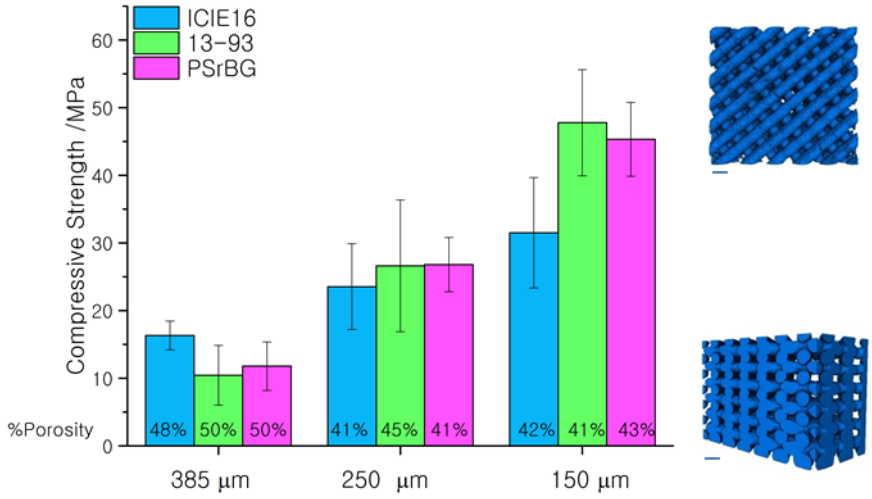

Figure 6: Compression testing results of scaffolds manufactured from ICIE16, PSrBG and 13-93 where x, y, z spacing was equal to 150, 250 and 385 µm, inserts show micro-CT volume renders of an ICIE16 scaffold with 150 µm spacing, scale bar is 300 µm.

All three glasses were printed at the same glass to ink ratio of 45 vol% of glass in 25 wt% Pluronic F-127, using nozzle diameters of 250, 410 and 610 µm, forming scaffolds with the same volume. Scaffolds were designed so that the pore size in x y and z was equal. Post sintering, the spacing between the scaffolds reduced to a modal channel size of 150 µm, 250 µm and 385 µm respectively (all within ± 5 µm). Figure 6 summarises the compressive strengths obtained for all three glasses at 3

channel sizes with their corresponding porosities. Reducing the nozzle diameter, and consequent channel size to 150 μm, led to an increase in strength up to 32.5 ± 8.1, 45.3 ± 5.5 and 47.7 ± 7.9 MPa for ICIE16, PSrBG and 13-93 respectively.

To understand the internal structure of the scaffolds, high resolution micro-CT was conducted on the i13 beam line at the Diamond light source. Figure 7 (a-c) shows the structure of the internal struts taking from a 2D slice, of ICIE16, PSrBG and 13-93 respectively. All three compositions were subject to internal strut porosity, it is hypothesised that this is due to the higher particle size used within this work. The larger particle size results in a lower packing density between particles within the strut structure. Although this facilitates the maintenance of the desired amorphous structure, it reduces the number of contact points, and consequently the amount of sintering via necking and viscous flow leading to internal strut porosity. Internal porosity can act as crack nucleation sites resulting in premature failure of the scaffolds. The level of sintering obtained within each glass varied. ICIE16 and 13-93 internal pores have become spherical, suggesting adequate viscous flow to minimise surface area. In contrast, the porosity within PSrBG remained non-spherical post sintering. Figure 7d is a 3D reconstruction of 13-93 scaffolds, highlighting the level of internal strut porosity, which was quantified to be 1.8 ± 0.2 %. Utilising the smaller particle size produced via jet milling may have reduced the amount of internal strut porosity within the scaffolds. However, lower volume fractions of glass would have been needed to be used within the ink to gain a ‘printable’ rheology, as well as crystallisation occurring during sintering, reducing the glasses highly bioactive nature and reproducibility.

Scaffolds with a channel size in x-y of 300 μm and z spacing of 330 μm with comparable porosity made from 13-93 glass, by Liu *et al.,* had reported strengths of 87 ± 9 MPa, which is nearly two times greater than those reported here. We hypothesise this is related to the difference in particle sizes used within this work, which caused the intra-strut porosity (Figure 7).

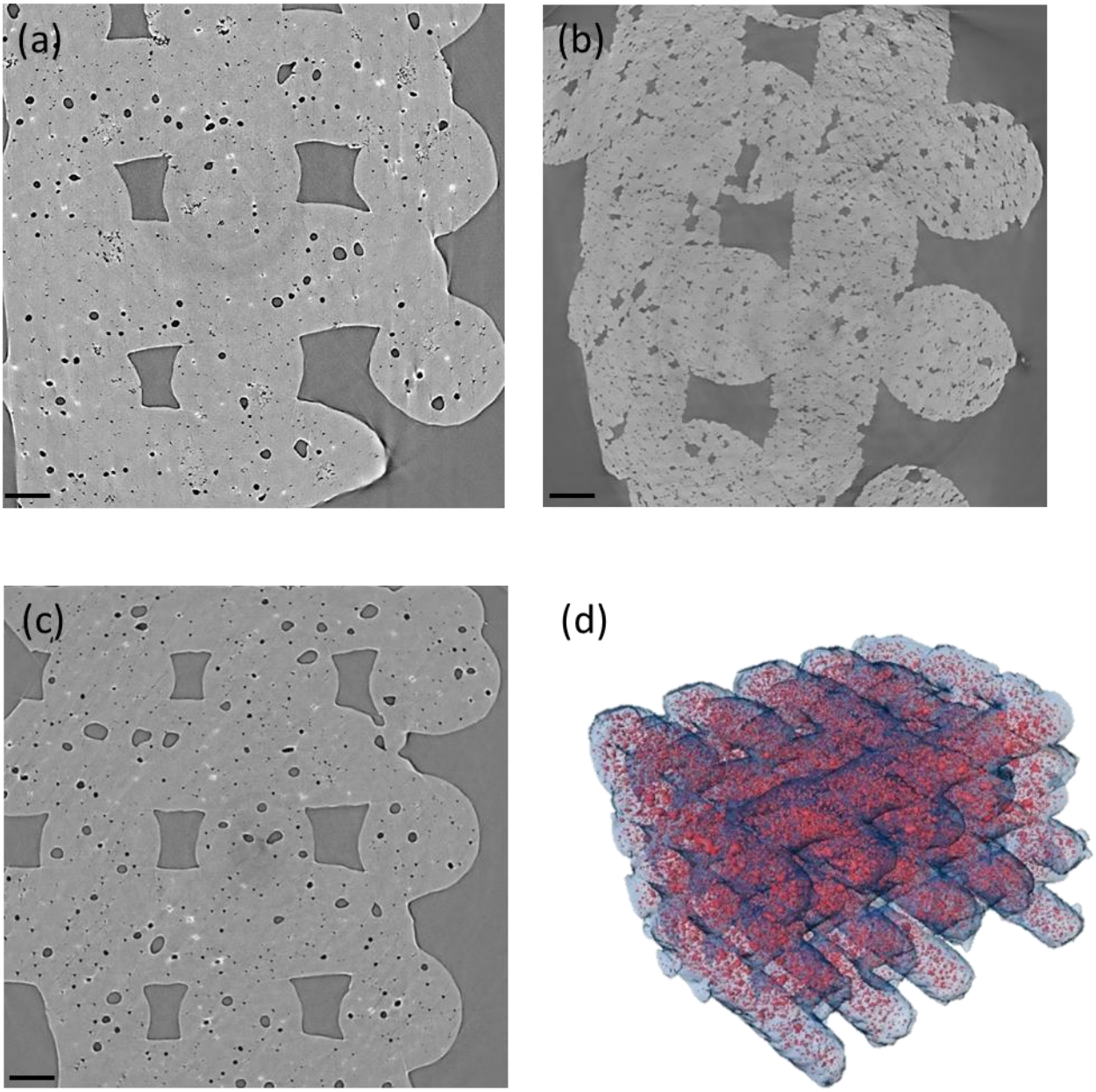

Figure 7: 2D micro-CT slices showing internal scaffold structure of (a) ICIE16, (b) PSrBG and (c) 13-93, scale bar is 100 µm. (d) 3D reconstruction of 13-93 internal strut porosity in red, encased within the struts (blue).

Conclusions

Bioactive glasses with silica contents <51.9 mol%, and modified network connectivities less than 2.58 were robocast into amorphous bioactive glass scaffolds suitable for bone repair. To be able to maintain the amorphous structure of the glasses used, a modal particle size 3 times greater than that of current literature was printed. There was a strong correlation between particle distribution and the force needed to extruded glass loaded inks and a reduction in Pluronic F-127 gelation temperature as glass loading in the inks increased. Due to the large particle size used, inherent strut porosity was found post sintering which limited the mechanical strength of the scaffolds produced.

Acknowledgements:

The 3D printer used within this work was funded via an EPSRC Grant for Graphene 3D networks (EP/K01658X/1). We thank Diamond Light Source for access to beamline I13-2 (MT13241-1) that contributed to the results presented here. This work was made possible by the facilities and support provided by the Diamond-Manchester Collaboration and the Research Complex at Harwell, funded in part by the EPSRC (EP/I02249X/1). Raw data available from rdm-enquiries@imperial.ac.uk.

References

1. Hench, L.L., *The story of Bioglass®.* Journal of Materials Science: Materials in Medicine, 2006. **17**(11): p. 967-978.
2. Jones, J.R., *Review of bioactive glass: From Hench to hybrids.* Acta Biomaterialia, 2013. **9**(1): p. 4457-4486.
3. Eqtesadi, S., et al., *A simple recipe for direct writing complex 45S5 Bioglass® 3D scaffolds.* Materials Letters, 2013. **93**(0): p. 68-71.
4. Chen, Q.Z., I.D. Thompson, and A.R. Boccaccini, *45S5 Bioglass-derived glass-ceramic scaffolds for bone tissue engineering.* Biomaterials, 2006. **27**(11): p. 2414-25.
5. Filho, O.P., G.P. La Torre, and L.L. Hench, *Effect of crystallization on apatite-layer formation of bioactive glass 45S5.* Journal of Biomedical Materials Research, 1996. **30**(4): p. 509-514.
6. Quintero, F., et al., *Laser Spinning of Bioactive Glass Nanofibers.* Advanced Functional Materials, 2009. **19**(19): p. 3084-3090.
7. Elgayar, I., et al., *Structural analysis of bioactive glasses.* Journal of Non-Crystalline Solids, 2005. **351**(2): p. 173-183.
8. O'Donnell, M.D. and R.G. Hill, *Influence of strontium and the importance of glass chemistry and structure when designing bioactive glasses for bone regeneration.* Acta Biomaterialia, 2010. **6**(7): p. 2382-2385.
9. Fagerlund, S., et al., *Phase composition and in vitro bioactivity of porous implants made of bioactive glass S53P4.* Acta Biomaterialia 2012. **8**(6): p. 2331-9.
10. Wu, Z.Y., et al., *Melt-derived bioactive glass scaffolds produced by a gel-cast foaming technique.* Acta Biomaterialia, 2011. **7**(4): p. 1807-1816.
11. Sriranganathan, D., et al., *Strontium substituted bioactive glasses for tissue engineered scaffolds: the importance of octacalcium phosphate.* Journal of Materials Science-Materials in Medicine, 2016. **27**(2): p. 10.
12. Fu, Q., et al., *Mechanical and in vitro performance of 13-93 bioactive glass scaffolds prepared by a polymer foam replication technique.* Acta Biomaterialia, 2008. **4**(6): p. 1854-64.
13. Liu, X., et al., *Mechanical properties of bioactive glass (13-93) scaffolds fabricated by robotic deposition for structural bone repair.* Acta Biomaterialia, 2013. **9**(6): p. 7025-34.
14. Deliormanlı, A.M. and M.N. Rahaman, *Direct-write assembly of silicate and borate bioactive glass scaffolds for bone repair.* Journal of the European Ceramic Society, 2012. **32**(14): p. 3637-3646.
15. Fu, Q., E. Saiz, and A.P. Tomsia, *Direct ink writing of highly porous and strong glass scaffolds for load-bearing bone defects repair and regeneration.* Acta biomaterialia, 2011. **7**(10): p. 3547-54.
16. Lewis, J.A., et al., *Direct Ink Writing of Three-Dimensional Ceramic Structures.* Journal of the American Ceramic Society, 2006. **89**(12): p. 3599-3609.
17. Smay, J.E., J. Cesarano, and J.A. Lewis, *Colloidal Inks for Directed Assembly of 3-D Periodic Structures.* Langmuir, 2002. **18**(14): p. 5429-5437.
18. Smay, J.E., et al., *Directed colloidal assembly of 3D periodic structures.* Advanced Materials, 2002. **14**(18): p. 1279-1283.
19. Eqtesadi, S., et al., *Robocasting of 45S5 bioactive glass scaffolds for bone tissue engineering.* Journal of the European Ceramic Society, 2014. **34**(1): p. 107-118.
20. Fu, Q., E. Saiz, and A.P. Tomsia, *Bioinspired Strong and Highly Porous Glass Scaffolds.* Advanced Functional Materials, 2011. **21**(6): p. 1058-1063.
21. Franco, J., et al., *Direct write assembly of calcium phosphate scaffolds using a water-based hydrogel.* Acta Biomaterialia, 2010. **6**(1): p. 218-228.

22. Chen, Q.Z., et al., *Surface functionalization of Bioglass-derived porous scaffolds.* Acta biomaterialia, 2007. **3**(4): p. 551-62.
23. Hill, R.G. and D.S. Brauer, *Predicting the bioactivity of glasses using the network connectivity or split network models.* Journal of Non-Crystalline Solids, 2011. **357**(24): p. 3884-3887.
24. Nommeots-Nomm, A., et al., *Highly degradable porous melt-derived bioactive glass foam scaffolds for bone regeneration.* Acta Biomaterialia, 2017. **57**: p. 449-461.
25. Compton, B.G. and J.A. Lewis, *3D-Printing of Lightweight Cellular Composites.* Advanced Materials, 2014. **26**(34): p. 5930-5935.
26. Kalyon, D.M., et al., *Rheological behavior of a concentrated suspension: A solid rocket fuel simulant.* Journal of Rheology (1978-present), 1993. **37**(1): p. 35-53.
27. Buscall, R., J.I. McGowan, and A.J. Morton-Jones, *The rheology of concentrated dispersions of weakly attracting colloidal particles with and without wall slip.* Journal of Rheology (1978-present), 1993. **37**(4): p. 621-641.
28. Chen, Z., et al., *Effect of particle packing on extrusion behavior of pastes.* Journal of Materials Science, 2000. **35**(21): p. 5301-5307.
29. Nommeots-Nomm, A., *3D printing versus foaming of melt-derived bioactive glasses for bone regeneration*. 2016, Imperial College London.
30. Fagerlund, S., et al., *T–T–T behaviour of bioactive glasses 1–98 and 13–93.* Journal of the European Ceramic Society, 2012. **32**(11): p. 2731-2738.
31. Vadnere, M., et al., *Thermodynamic studies on the gel-sol transition of some pluronic polyols.* International Journal of Pharmaceutics, 1984. **22**(2–3): p. 207-218.
32. Herschel, W.B., R., *Konsistenzmessungen von Gummi-Benzollosungen.* Kolloid Zeitschrift, , 1926. **39**: p. 291–300.
33. Cohn, D., A. Sosnik, and S. Garty, *Smart Hydrogels for in Situ Generated Implants†.* Biomacromolecules, 2005. **6**(3): p. 1168-1175.
34. Lenaerts, V., et al., *Temperature-dependent rheological behavior of Pluronic F-127 aqueous solutions.* International Journal of Pharmaceutics, 1987. **39**(1–2): p. 121-127.
35. Conrad, J.C. and J.A. Lewis, *Structure of colloidal gels during microchannel flow.* Langmuir, 2008. **24**(15): p. 7628-7634.
36. Feilden, E., et al., *Robocasting of structural ceramic parts with hydrogel inks.* Journal of the European Ceramic Society, 2016. **36**(10): p. 2525-2533.